

# On the mechanisms underlying the depolarization block in the spiking dynamics of CA1 pyramidal neurons

Daniela Bianchi · Addolorata Marasco · Alessandro Limongiello ·  
Cristina Marchetti · Helene Marie · Brunello Tirozzi · Michele Migliore

Received: 11 October 2011 / Revised: 11 January 2012 / Accepted: 13 January 2012 / Published online: 5 February 2012  
© Springer Science+Business Media, LLC 2012

**Abstract** Under sustained input current of increasing strength neurons eventually stop firing, entering a depolarization block. This is a robust effect that is not usually explored in experiments or explicitly implemented

or tested in models. However, the range of current strength needed for a depolarization block could be easily reached with a random background activity of only a few hundred excitatory synapses. Depolarization block may thus be an important property of neurons that should be better characterized in experiments and explicitly taken into account in models at all implementation scales. Here we analyze the spiking dynamics of CA1 pyramidal neuron models using the same set of ionic currents on both an accurate morphological reconstruction and on its reduction to a single-compartment. The results show the specific ion channel properties and kinetics that are needed to reproduce the experimental findings, and how their interplay can drastically modulate the neuronal dynamics and the input current range leading to a depolarization block. We suggest that this can be one of the rate-limiting mechanisms protecting a CA1 neuron from excessive spiking activity.

---

**Action Editor:** Frances K. Skinner

---

D. Bianchi and A. Marasco contributed equally to this work.

D. Bianchi (✉) · B. Tirozzi  
Department of Physics, University of Rome “La Sapienza”,  
Piazz. le A. Moro 2, 00185, Rome, Italy  
e-mail: danielabianchi12@gmail.com,  
daniela.bianchi@roma1.infn.it

B. Tirozzi  
e-mail: brunello.tirozzi@roma1.infn.it

A. Marasco · A. Limongiello  
Department of Mathematics and Applications “R.  
Caccioppoli”, University of Naples Federico II, Via Cintia,  
80126, Naples, Italy

A. Marasco  
e-mail: marasco@unina.it

A. Limongiello  
e-mail: alessandro.limongiello@unina.it

C. Marchetti · H. Marie  
European Brain Research Institute “Rita Levi-Montalcini”,  
Via del Fosso di Fiorano 64, 00143, Rome, Italy

C. Marchetti  
e-mail: c.marchetti@ebri.it

H. Marie  
IPMC - CNRS UMR6097, 06560 Valbonne, France  
e-mail: marie@ipmc.cnrs.fr

M. Migliore  
Institute of Biophysics National Research Council,  
via U. La Malfa 153, 90146 Palermo, Italy  
e-mail: michele.migliore@cnr.it

**Keywords** Depolarization block · CA1 pyramidal neuron · Bifurcation analysis · Kinetics

## 1 Introduction

In response to prolonged depolarizing current steps, different classes of neurons display specific firing characteristics, such as a regular train of Action Potentials (APs) with more or less adaptation, delayed responses, or bursting. In general, one or more specific ionic transmembrane currents underlie the different firing patterns (Hemond et al. 2008), and pathological or physiological modulation of these channels can greatly change the firing behavior of a neuron. In this paper,

we focus on a particular behavior of pyramidal CA1 neurons. In response to constant somatic current steps of increasing strength,  $I_{inj}$ , these neurons fire regularly, with some frequency adaptation. Experimentally, values of  $I_{inj}$  much beyond the range of the linear increase for the I/O curve are rarely tested. It is known that in this input range these neurons eventually stop firing, reaching a depolarization block in which the membrane potential, during the current injection, remains constant, generally around  $-40$  mV. This condition has not been further explored experimentally or theoretically, probably because it is considered unphysiological. However, simple considerations reveal that it can be reached for a level of synaptic activity well within the physiological range that can be expected *in vivo*. We think that this is a potentially important issue that can significantly affect the behavior of neuronal networks. However, very little is known about the ability of a model to reproduce the depolarization block as observed experimentally. For this reason, in this work we have explored the properties of both a realistic and a reduced model of CA1 pyramidal neurons, highlighting the conditions under which a neuron is able to enter a depolarization block. The model suggests experimentally testable predictions on which mechanisms and kinetic properties are responsible for the depolarization block observed in the experiments and on how these could be modulated. The results indicate how to include this, so far ignored but important feature, into future implementation of neurons and networks.

The paper is organized in five sections including the introduction. In Section 2, a description of morphological and single-compartment models of a CA1 pyramidal neuron are presented. Section 3 presents experimental results and develops a quantitative and qualitative analysis of the above models, with special attention to the main mechanisms underlying the depolarization block, a stability analysis of the steady-state values, bifurcation diagrams for the single-compartment model, and its behavior in the presence of synaptic input. Section 4 deals with a discussion of the results. In the [Appendix](#), we include the equations for ionic currents and a more detailed description of the mathematical analysis used for the model.

## 2 Materials and methods

### 2.1 Experiments

Electrophysiological recordings were obtained from CA1 pyramidal neurons of P19–P24 Sprague-

Dawley rats. Animals were deeply anesthetized with isoflurane inhalation, decapitated, and the brains were quickly removed and immersed in ice-cold cutting solution containing (in mM) 2.5 KCl, 1.25  $\text{NaH}_2\text{PO}_4$ , 10  $\text{MgSO}_4$ , 0.5  $\text{CaCl}_2$ , 26  $\text{NaHCO}_3$ , 234 Sucrose, 11 Glucose (saturated with 95%  $\text{O}_2$  and 5%  $\text{CO}_2$ ). 250  $\mu\text{m}$  thick coronal hippocampal slices were made and kept, after the dissection, in regular artificial cerebro-spinal fluid (ACSF), at a temperature of  $34^\circ\text{C}$  for 1 h, and then at room temperature. ACSF was composed of (in mM) 119 NaCl, 2.5 KCl, 1.25  $\text{NaH}_2\text{PO}_4$ , 1.3  $\text{MgSO}_4$ , 2.5  $\text{CaCl}_2$ , 26  $\text{NaHCO}_3$ , 11 Glucose, gassed with 95%  $\text{O}_2$  plus 5%  $\text{CO}_2$ . For recordings, slices were submerged in oxygenated ACSF at a temperature of  $30$ – $32^\circ\text{C}$ . Whole-cell patch clamp recordings were obtained from visually identified CA1 pyramidal cells in current clamp mode (intracellular solution, in mM: 70 Kgluconate, 70 KCl, 10 HEPES, 1 EGTA, 0.05  $\text{MgCl}_2$ , pH = 7.3, osmolarity 290 mOsm), using a Multiclamp 700B amplifier (Molecular Devices, Sunnyvale, CA, USA). Data were digitized with a Digidata 1440A at 20 kHz sampling, filtered at 10 kHz and recorded with pClamp 10.2 (Molecular Devices, Sunnyvale, CA, USA). Current steps of 1 s duration were delivered through the same amplifier in steps of 50 pA. Spike count analysis was performed with Clampfit 10.2 with a threshold based search. Threshold for spike detection was chosen at  $-20$  mV. Average ( $\pm$ SD) resting membrane potential was  $-71.2 \pm 3.6$  mV ( $n = 12$ ) and input resistance  $112 \pm 38$  M $\Omega$  ( $n = 9$ ). All neurons tested ( $n = 12$ ) exhibited a depolarization block, defined as a silent period of time starting in the course of the current injection, lasting until the end of the pulse, and during which the membrane potential was approximately constant. The threshold current to reach the depolarization block was defined as the value of the current injection,  $I_{th}$ , for which the cell exhibited the maximum number of spikes. The average equilibrium value during the depolarization block,  $V_{eq}$ , was calculated by averaging the membrane potential over the last 100 ms of a current pulse 50 pA above  $I_{th}$ .

### 2.2 Morphological model of CA1 pyramidal neuron

We performed our simulations using the NEURON simulation environment (version 7.1, (Hines and Carnevale 2003)) and a CA1 pyramidal neuron implemented by merging the model by Poirazi et al. (2003b) (ModelDB accession number 20212), which includes a large set of currents experimentally observed in these neurons, and the model by Shah et al. (2008) (ModelDB accession number 112546), which includes

**Table 1** Maximal conductances  $\bar{g}$  of the currents included in the morphological model expressed in mS/cm<sup>2</sup>

Name of current	Soma	Apical trunk	Apical dendrites	Basal dendrites	Axon
$I_{NaT}$	35	35	35	12.5	35
$I_{Kdr}$	15	15	15	9	15
$I_h$	0.018	*	*	0.018	—
$I_{KAprox}$	0.5	**	**	8	0.5
$I_{KAdist}$	0.5	**	**	8	0.5
$I_{KM}$	1	—	—	—	3
$I_{sAHP}$	15	*	*	—	—
$I_{mAHP}$	247.5	*	*	—	—
$I_{CaR}$	0.1	0.3	*	—	—
$I_{CaL}$	0.5	0.632	*	—	—
$I_{CaT}$	0.05	*	*	—	—
$I_{Nap}$	—	0.0028	*	—	—

\* means that  $\bar{g}$  follows the rule shown in Poirazi et al. paper, \*\* means that  $\bar{g}$  increases linearly with the distance from soma

updated kinetics and distributions of dendritic channels (reviewed in Migliore and Shepherd 2002, 2005). Passive properties, peak conductance and dendritic distribution for each channel were adapted from their original values to take into account the specific set of experimental traces used in this work, and are reported in Tables 1 and 2. The kinetic details of transient sodium ( $NaT$ ), delayed-rectifier potassium ( $K_{DR}$ ), m type potassium (M), medium fast calcium dependent potassium ( $mAHP$ ) currents are described in the Appendix, in Section “Ionic currents”. The remaining currents are those described in the supplementary data of Poirazi et al. (2003a) (Supplemental data at <http://www.neuron.org/cgi/content/full/37/6/977/DC1>). Unless explicitly stated otherwise, in all cases  $NaT$  activation was shifted  $-5$  mV in the axon with respect to the soma (Colbert and Pan 2002). The NEURON model files are available on ModelDB (<http://senselab.med.yale.edu/ModelDB/>), accession number 143719.

### 2.3 Single-compartment model of CA1 pyramidal neuron

In order to make a more detailed analysis of the processes leading to a depolarization block, we reduced the morphological model to a single compartment in two stages. Starting from the full model, we first considered a model obtained by deleting all compartments except the soma. Then we found the parameters that best

reproduced the qualitative features of the experimental data including the depolarization block. In this model, the current balance equation of the somatic membrane potential  $V$  depends, in addition to the injected current  $I_{inj}$  and leakage  $I_{leak}$ , on the ten ionic currents listed in the Appendix

$$C_m \frac{dV}{dt} = -I_{NaT} - I_{K_{DR}} - I_{K_M} - I_{K_A} - I_{CaT} - I_{CaR} - I_{CaL} - I_h - I_{sAHP} - I_{mAHP} - I_{leak} + I_{inj}. \quad (1)$$

where  $C_m = 1 \mu\text{F}/\text{cm}^2$  is the specific capacitance of the membrane, and all currents are in  $\mu\text{A}/\text{cm}^2$  (Koch 1999). Then, closing the membrane equation (1) with the dynamics of the gating variables of the ionic currents, and the intracellular  $\text{Ca}^{2+}$  concentration (see Section “Mathematical description of the somatic model”), the model is described by a system of seventeen nonlinear ordinary differential equations, instead of the 5,563 nonlinear partial differential equations needed to model the full morphology. However, since the model is described by a system of nonlinear equations and most of them depend on piecewise functions, the stability analysis of the steady-state values, and all suitable bifurcation diagrams were obtained by custom procedures written in *Mathematica* (Marasco and Romano 2001). In all simulations, initial conditions for all variables were those corresponding to their steady-state value at the resting potential

**Table 2** Passive properties of the morphological model

Parameter	Soma	Apical trunk	Apical dendrites	Basal dendrites	Axon
$R_m$ ( $\Omega/\text{cm}^2$ )	20,000	36,900	36,900	46,000	28,000
$R_a$ ( $\Omega\text{cm}$ )	150	150	150	150	50
$C_m$ ( $\mu\text{F}/\text{cm}^2$ )	1	1.192	1.192	1.144	1
$E_{pas}$ (mV)	$-70$	$-70$	$-70$	$-70$	$-70$

( $-70$  mV), and the input current used to model the whole-cell current-clamp experiments was scaled by a factor  $1/(\pi d_{\text{Soma}} L_{\text{Soma}})$ , to take into account the membrane capacitance of the cell and to convert the experimental input (in nA) into units consistent with Eq. (1) ( $\mu\text{A}/\text{cm}^2$ ).

### 3 Results

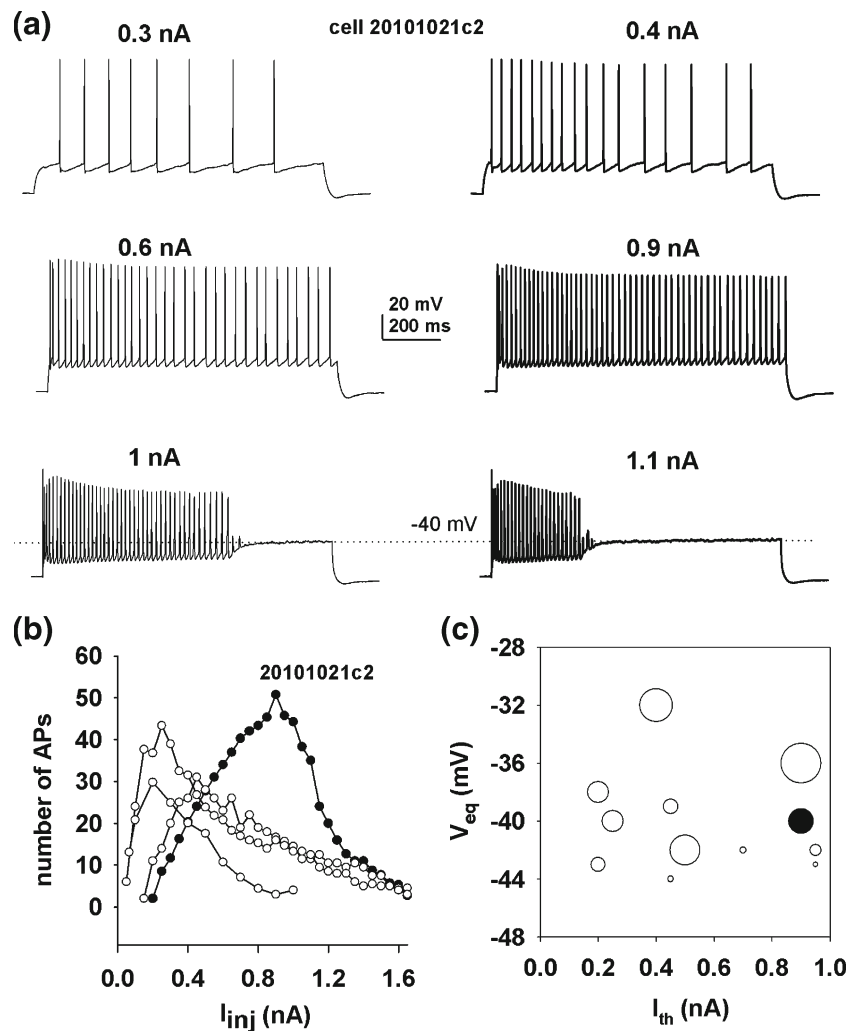
Typical experimental findings obtained from a CA1 pyramidal neuron (cell 20101021c2) are shown in Fig. 1(a) for 1 s depolarizing current steps injected in the soma.

For current intensities up to  $0.9$  nA, the neuron exhibits some spike adaptation, but fires throughout the duration of the current step. For stimulation intensities of  $1$  nA and above, the neuron stops firing while the

current is still present in the soma. Total number of spikes fired during the  $1$  s step decreases as the input current increases. All neurons tested ( $n = 12$ ) exhibit this behavior, but the value of the injected current at which the number of spikes starts decreasing is in general different for each cell. In Fig. 1(b) we report the average number of spikes for a  $1$  s current injection for 4 representative cells. The range of  $I_{\text{th}}$  values at which a depolarization block occurs is between  $200$  pA and  $0.95$  nA (average  $600 \pm 300$  pA,  $n = 12$ ), with an average  $V_{\text{eq}}$  of  $40.1 \pm 3.4$  mV ( $n = 12$ ), and there is no correlation between  $V_{\text{eq}}$  or  $I_{\text{th}}$  and the input resistance, the resting potential, or the number of spikes before the block (Pearson's correlation test,  $p$ -value  $> 0.1$  in all cases). The large variability observed, illustrated in Fig. 1(c), is not surprising and reflects cell-to-cell variability in morphological properties (Samsonovich and Ascoli 2005) and the large activity-dependent changes in channel density, activation/inactivation, and kinetic

**Fig. 1** CA1 neurons spiking patterns in response to increasing current steps.

(a) Set of somatic membrane potential recorded from cell 20101021c2 in whole-cell current clamp configuration in response to increasing current steps. (b) Average number of APs recorded from different cells in response to  $1$  s somatic current injection, calculated from 3 step repetitions; for clarity, results from only 4 cells are shown; *black symbols* represent results from cell 20101021c2. (c) Equilibrium values of the somatic membrane potential at depolarization block ( $V_{\text{eq}}$ ) as a function of  $I_{\text{th}}$  for all cases; bubble size is proportional to the number of APs (between 13 and 82) elicited at  $I_{\text{th}}$ ; the *black bubble* represents cell 20101021c2



properties occurring in any given neuron during its lifetime (reviewed in Remy et al. 2010).

In modeling these data, in addition to qualitatively matching the number of APs elicited as a function of  $I_{inj}$  before the depolarization block, we were especially interested in reproducing the following properties:

- below a threshold value of  $I_{inj}$ , the neuron fires a regular, weakly adapting, train of APs for the entire duration of the current step;
- beyond a threshold value of  $I_{inj}$ , and during the current step, the APs amplitude decreases to zero and the membrane potential reaches an equilibrium point which lies in a range between  $-40$  mV and  $-35$  mV;
- beyond a threshold value of  $I_{inj}$ , the overall number of spikes decreases with increasing current.

### 3.1 Main mechanisms underlying the depolarization block

Our first main aim was to determine which mechanism is responsible for the depolarization block. We first considered the full morphology used in the paper by Poirazi et al. (2003b) including only the basic mechanisms responsible for AP firing (from Shah et al. 2008, i.e.  $NaT$ ,  $K_{DR}$  and passive currents), at uniform density throughout the somatodendritic region and with parameters fixed at their somatic value. The membrane potential response for two values of  $I_{inj}$ , shown in Fig. 2, demonstrates that under these conditions the model is able to generate a depolarization block, although the membrane potential reaches an equilibrium point at a higher level with respect to the experiments. Since several experimental findings suggest that the activation curve of  $Na^+$  and  $K^+$  conductances in CA1 pyramidal neurons can be easily modulated by activity-dependent processes (Gasparini and Magee 2002; Hoffman and Johnston 1998), we tested different values for the midpoint of the activation curve of  $NaT$  and  $K_{DR}$ , i.e.  $V_{mNaT}^{1/2}$  and  $V_{mKDR}^{1/2}$ . We found that the phenomenon was very robust, and relatively large shifts (up to 5 mV) in the activation curves did not result in qualitative differences (not shown). To investigate how and to what extent the ability of a neuron to enter a depolarization block depends on the interaction between the activation/inactivation properties of the two active channels ( $NaT$ ,  $K_{DR}$ ), we manually explored several different combinations of their activation curve midpoints, deferring a more systematic and detailed mathematical analysis to the single-compartment case (see Section 3.2).

We found that the necessary relations between the two channels are that:

- $V_{mKDR}^{1/2}$  should be shifted to the right with respect to the  $V_{mNaT}^{1/2}$ ,
- the  $NaT$  window current (generated in the membrane potential range where the inactivation and activation steady-state curves overlap) must be relatively small.

The reasons for these relations can be easily understood: a high window current generates a relatively large sodium current, which would bring the neuron to a depolarization block for any suprathreshold current injection, whereas a low voltage for  $K_{DR}$  activation would more easily repolarize the neuron after each AP, preventing the depolarization block. Both conditions are met in the model for  $NaT$  and  $K_{DR}$  by Shah et al. (2008), see Fig. 2(c), whereas using  $NaT$  and  $K_{DR}$  from Poirazi et al. (2003b) the depolarization block could not be achieved, as shown in Fig. 3(a). In this case, neither condition is fulfilled, and the number of APs monotonically increased up to values of  $I_{inj}$  well beyond the physiological range, as shown in Fig. 3(b) and (c).

Additional insights into the dynamics leading to the depolarization block can be gained by considering the time course of activation/inactivation for  $NaT$  and  $K_{DR}$  (insets in Figs. 2(a) and 3(c)). For the model in Fig. 2, the block appears to be caused by the incomplete return of the  $NaT$  channel to a fully deinactivated state between spikes (compare the traces for  $Na^+$  inactivation in Fig. 2(a), top and bottom). This effect, coupled with a small activation of  $K_{DR}$  (which is unable to repolarize the membrane), generates a progressive reduction in the  $NaT$  channel availability to generate action potentials at full amplitude. By contrast, the larger window current in the model of Fig. 3 generates a small but sustained  $NaT$  current that is partially counteracted by a full  $K_{DR}$  activation, with an overall dynamics that avoids the depolarization block. In this context, it should be noted that any additional inward current, such as a persistent  $Na^+$  current, would facilitate the depolarization block. These kinds of currents should be considered as extra mechanisms able to modulate the dynamics to the block. However, they are not necessary, since the interaction between  $NaT$  and  $K_{DR}$  currents is sufficient to capture the main effect. Taken together, these results confirmed that the mechanisms necessary and sufficient to enter a depolarization block are  $NaT$  and  $K_{DR}$ . Using different CA1 morphologies (not shown) the block was still achieved with only minor differences in the number of spikes.



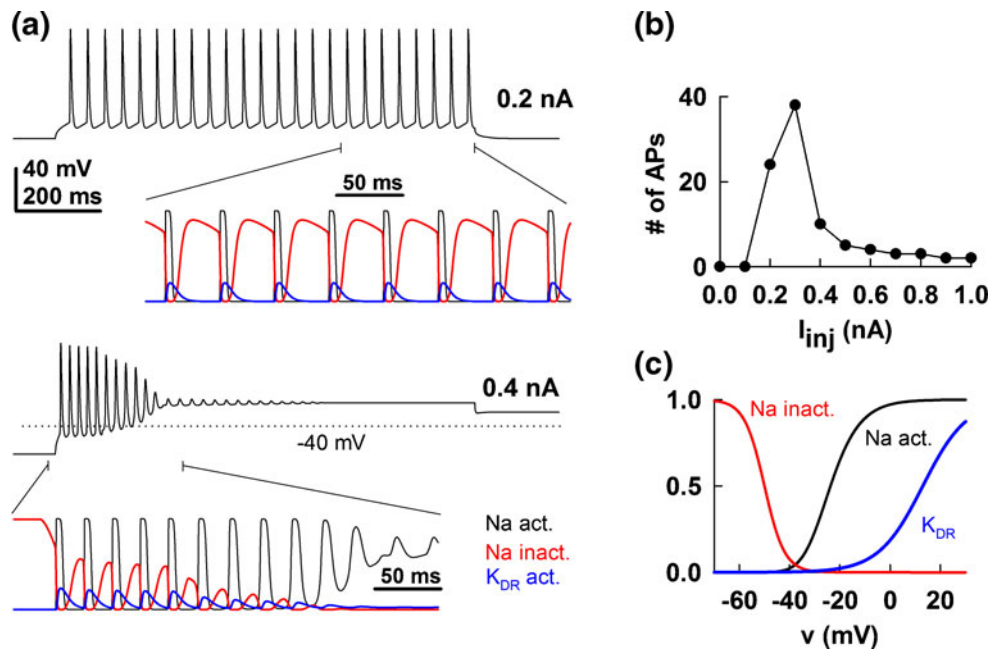


**Fig. 2** The  $NaT$  and  $K_{DR}$  currents are sufficient to achieve the depolarization block. **(a)** Model response to 0.2 nA and 0.4 nA depolarizing pulse of external current injected in the soma. Somatic membrane potential during the entire simulation, and activation and inactivation variables for  $NaT$  and  $K_{DR}$  at the end (top) or at the beginning (bottom) of the current injection. In this

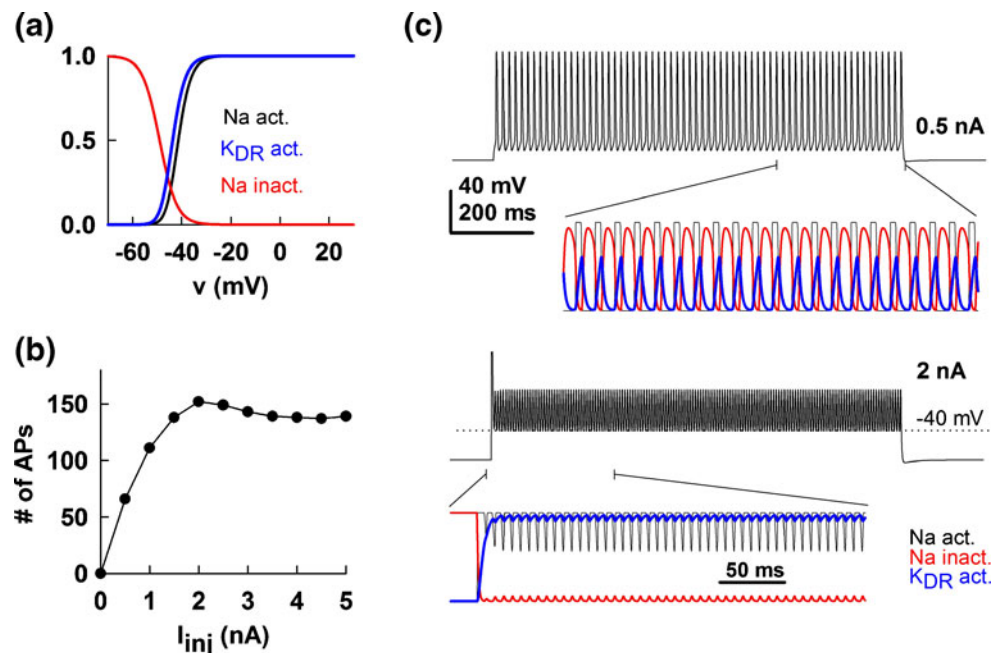
model,  $NaT$ ,  $K_{DR}$  and leak currents are uniformly distributed in the soma and dendrites. **(b)** Number of APs triggered in response to increasing depolarizing external current injected in the soma. **(c)** Voltage-dependence of the steady-state for the activation and inactivation curves of  $NaT$  and  $K_{DR}$

### 3.1.1 Results using a full realistic model

Although a suitable formulation for the  $NaT$  and  $K_{DR}$  currents is needed to achieve depolarization block, they

are of course not enough to reproduce the major experimental features that we were interested to model. For example, the depolarization block level was around  $-20$  mV rather than  $-40$  mV as in the data, suggesting

**Fig. 3** Specific relations between activation/inactivation properties of  $NaT$  and  $K_{DR}$  currents are needed for the depolarization block. **(a)** Steady-state activation and inactivation of  $NaT$  and  $K_{DR}$  (from Poirazi et al. 2003b) that cannot reproduce the depolarization block. **(b)** Number of APs triggered in response to increasing somatic current injection. **(c)** Model response to 0.5 nA and 3 nA. Somatic membrane potential during the entire simulation, and activation and inactivation variables for  $NaT$  and  $K_{DR}$  at the end (top) or at the beginning (bottom) of the current injection



that another  $K^+$  current might be involved. We found that both the  $K_M$  or the  $K_{mAHP}$  were able to reduce  $V_{eq}$  to that observed in the experiments, as shown in Fig. 4 for two representative current inputs in the two cases, and that their peak conductance is able to modulate  $V_{eq}$  over the entire experimental range (Fig. 4(a), inset).

To test our full model over a large range of current injections, we choose as a reference set of experimental traces those from cell 20101021c2, which also had a  $V_{eq}$  corresponding to the average value from all cells (i.e.  $-40$  mV, see black circle in Fig. 1(c)). In order to fine tune the model and reproduce the spike number and timing for this particular experimental case, we explored the parameter space of the model by hand in the presence of the full set of currents. The best agreement with experiments was found with minor modifications, with respect to their original values, of  $NaT$ ,  $K_M$ , and  $K_{mAHP}$  kinetics. The final set of parameters is reported in Table 3. The results, shown in Fig. 5, demonstrate that the model agrees well with all the conditions we defined to characterize the experimental recordings, i.e.:

- below a critical value of  $I_{inj}$  (0.9 nA in this case) the neuron fires a regular, weakly adapting, train of APs for the entire duration of the current step, Fig. 5(a) (top and middle traces);
- beyond a critical value of  $I_{inj}$ , and during the current step, the AP amplitude decreases to zero and the membrane potential reaches an equilibrium point which lies in a range between  $-40$  mV and  $-35$  mV, and the overall number of spikes decreases with increasing current, Fig. 5(a) (bottom traces).

The time course of the state variables for  $NaT$  and  $K_{DR}$  (Fig. 5(a), bottom) confirmed the same dynamics observed for the simplified model (Fig. 2). Finally, the number of spikes as a function of the input current (Fig. 5(b)) is in reasonable agreement with the experiments, especially below the depolarization block.

Since each cell enters the depolarization block state at different values of  $I_{th}$ , we investigated if some passive or morphological properties can explain the large observed variability. A series of simulations was carried out by systematically altering (by  $\pm 40\%$ ) either the dendrites' diameter or the specific membrane resistance, with or without adjusting the specific membrane capacitance to maintain the same membrane time constant (we will refer to the two cases as  $R_{m\tau}$  or  $R_m$ , respectively). As shown in Fig. 6, our model suggests a direct correlation between  $I_{th}$  and  $R_{m\tau}$ ,  $R_m$ , and the average dendrites' diameter. The  $I_{th}$  increases or decreases following changes in these parameters. Since they independently modulate in a non-linear way the input resistance ( $R_N$ ) of a neuron, the lack of correlation in the experimental findings with the  $I_{th}$  can be easily explained, since different neurons will have an uncorrelated combination of average dendrites' diameter and membrane resistance. However, a change of  $R_N$  obtained in any given neuron through a manipulation of only one parameter should affect the  $I_{th}$  in a predictable way. An experimentally testable prediction of the model is thus to change the  $R_N$  by blocking the  $I_{th}$  current, a well known determinant of the input resistance of CA1 neurons (Magee 1998) (but not, of course, of the membrane area). This should change  $I_{th}$  in the same way as found in the model for changes in  $R_m$  (Fig. 6, right, triangles).

**Fig. 4** The  $K_M$  or  $K_{mAHP}$  currents can modulate the equilibrium value of the membrane potential at the depolarization block. (a) Somatic membrane potential to a 0.3 and 0.7 nA current injection when  $K_M$  was included in the model of Fig. 2; inset on the right plot shows  $V_{eq}$  for different values of the peak  $K_M$  conductance. (b) Somatic membrane potential to 0.25 and 0.6 nA when  $K_{mAHP}$  and  $CaL$  currents were included in the model of Fig. 2

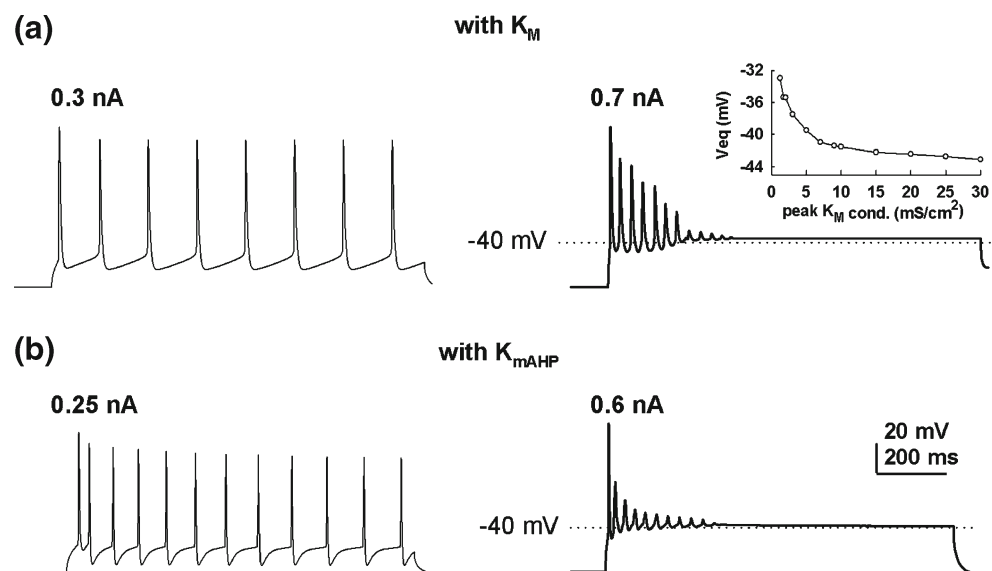
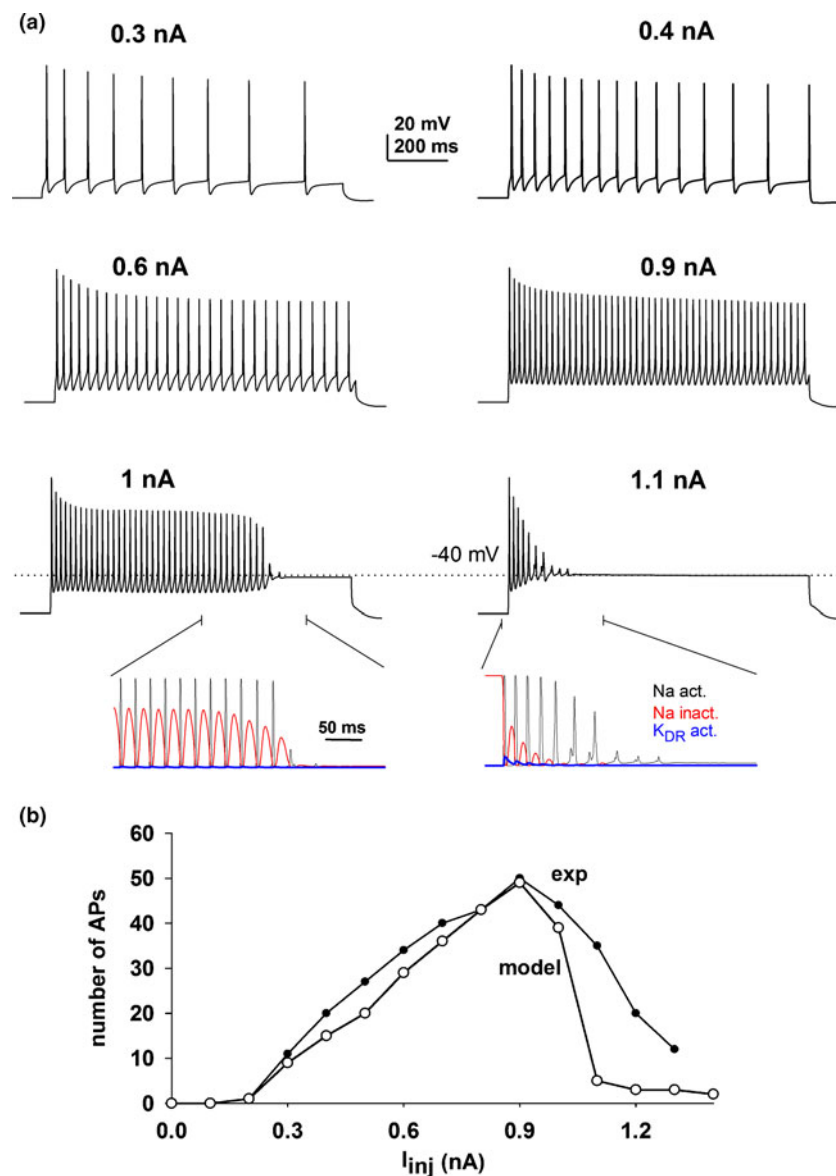


**Table 3** Values of the parameters best fitting the experimental traces of cell 20101021c2 (only changes with respect to the original model are reported)

Parameter	Soma	Apical trunk	Apical dendrites	Basal dendrites	Axon
$V_{mNaT}^{1/2}$ (mV)	−25	−25	−23	−23	−30
$k_{mNaT}$ (mV)	7.2	7.2	7.2	7.2	7.5
$V_{hNaT}^{1/2}$ (mV)	−50	−50	−50	−50	−54
$k_{hNaT}$ (mV)	2	2	2	2	1
$V_{mKM}^{1/2}$ (mV)	−42	—	—	—	−42
$k_{mKM}$ (mV)	−4	—	—	—	−4
$\bar{\tau}_{mKM}$ (ms)	$\frac{1}{0.04}$	—	—	—	$\frac{1}{0.04}$
$\tilde{k}_{mKM}$ (mV)	$\frac{-1}{0.1512}$	—	—	—	$\frac{-1}{0.1512}$
$\gamma_{mKM}$	0.7	—	—	—	0.7
$d_1(mAHP)$	1	1	1	1	1
$d_2(mAHP)$	1.5	1.5	1.5	1.5	1.5

**Fig. 5** Simulations findings using the full model.

(a) Somatic membrane potential for increasing current injections; activation and inactivation parameters for  $NaT$  and  $K_{DR}$  current are shown for the two values of  $I_{inj}$  leading to the block. (b) Number of action potentials, triggered in the model and in the experiments (cell 20101021c2), in response to an increasing depolarizing external current injected in the soma





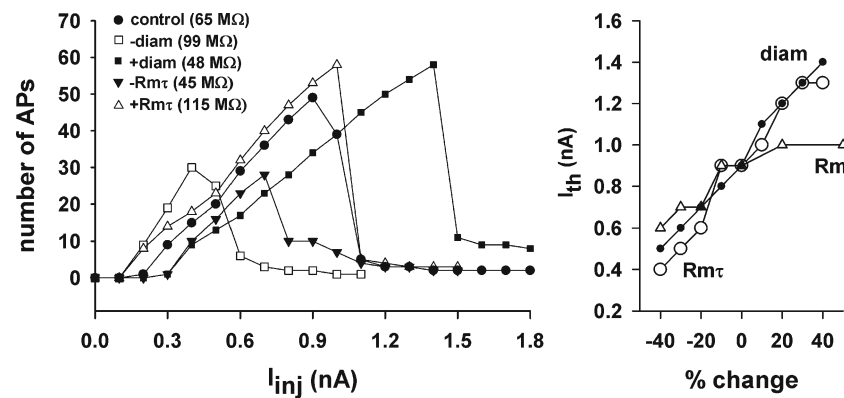


**Fig. 6** The input current at which depolarization block also depends on morphological and passive properties. *Left* Number of APs triggered in response to increasing depolarizing current injected in the soma, obtained by increasing (+) or decreasing

(–) either the dendrites' diameter or the  $R_{m\tau}$  (see text for definition). *Right*  $I_{th}$  vs. relative changes of dendrites' diameter,  $R_{m\tau}$  or  $R_m$

### 3.1.2 Morphological model with synaptic input

We next tested our model behavior under synaptic inputs. It should be stressed that this is a significant issue. Neurons *in vivo* receive the vast majority of their excitatory input from synapses in the dendrites rather than in the soma. It was thus important to test if the depolarization block can be also reached during sustained synaptic activity. For this reason, we used a variable number of dendritic excitatory synapses (AMPA and NMDA type, at a 2:1 ratio and peak AMPA conductance of 0.7 nS). Synapses were randomly placed on basal and apical dendrites. Following the experimentally estimated average distribution for a CA1 pyramidal neuron (Megias et al. 2001), 40% of them were distributed in the basal and 60% in the apical oblique dendrites. Most synapses (80%) contained both AMPA and NMDA components, and 20% only NMDA (Marie et al. 2005). They were independently and randomly activated at 50 Hz (in the gamma range), according to a Poisson distribution. The average number of somatic APs as a function of the number of activated synapses was calculated from ten simulations in which synaptic location and activation times were randomly redistributed. Typical somatic traces are plotted in Fig. 7, and show that the depolarization block can be reached during a sustained activation of about 180 synapses. Considering that the average peak miniature excitatory synaptic current in CA1 pyramidal neurons has been estimated to be 13–25 pA (Andrasfalvy and Magee 2001; Ito and Schuman 2009), our synapses correspond to about 500–1,000 real inputs, less than 3% of the total number of excitatory inputs (Megias et al. 2001).

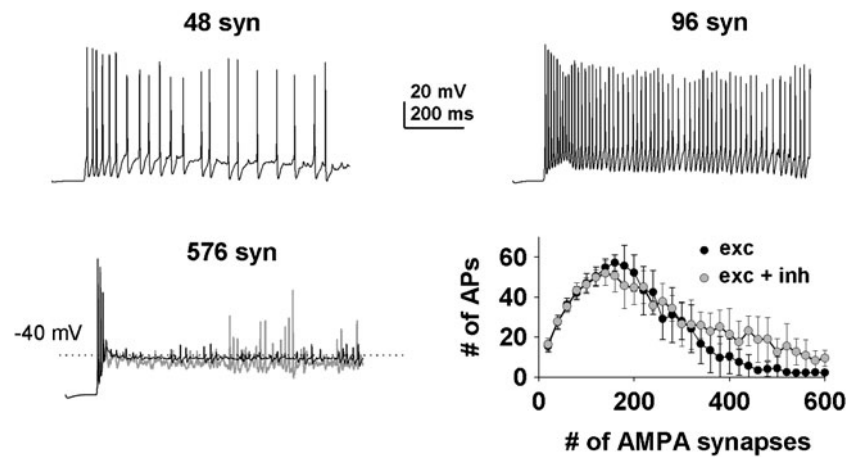
Neuronal activity *in vivo* has also an inhibitory component that, in principle, could have some influence

on the depolarization block. For this reason, we have carried out a set of simulations including also inhibitory GABA<sub>A</sub> synapses (modeled as in Poirazi et al. 2003b), activated according to the same protocol used for the excitatory synapses, and using a peak conductance and distribution consistent with experimental data (Megias et al. (2001) for distribution and proportion with respect to excitatory synapses, Jiang et al. (2000) for peak conductance). In particular, the peak conductance was set to 5 nS, and the total number of inhibitory synapses was 5.6% of the excitatory ones, 7% of them distributed in the soma, 40% in the basal, and the rest in the apical dendrites. The results (Fig. 10, bottom panels, grey traces) show that inhibitory synapses do not result in a substantial change, under the simplified conditions used in our case. Of course, a deeper analysis on the relative contribution of excitatory and inhibitory inputs under different conditions in terms of number, distribution (dendritic, somatic, etc), and stimulation (frequency, delay, activation pattern, etc), can give a more detailed picture of their interaction. This kind of analysis, however, was out of the scope of this paper.

### 3.1.3 The somatic reduced model

Simulations using large neuronal networks are rarely carried out using morphologically realistic reconstructions, since computational times increase dramatically with network size. A suitable reduction of a full morphological neuron to a single compartment model is thus highly desirable. To this end, and to be able to analyze in more detail the model's dynamics, we reduced our full morphology to a single compartment in two sequential stages: (1) by just deleting all compart-

**Fig. 7** Simulation findings using synaptic inputs. Typical somatic membrane potential during sustained random synaptic activity (Poisson distribution) of different number of synapses, and number of somatic action potentials triggered in response to an increasing number of synapses. Traces and symbols in *black* show results using only excitatory inputs, those in *grey* show results with excitatory and inhibitory inputs



ments except the soma, maintaining all of its properties unchanged with respect to the full morphology, and (2) by adapting the peak conductances and the somatic capacitance to qualitatively model the experimental data, including the depolarization block phenomenon.

The stability properties of the membrane potential  $V$  versus  $I_{inj}$  for the former case are shown in Fig. 8. Both cyan and blue points refer to asymptotically stable equilibria, whereas the red points refer to unstable equilibria (see Section “[Mathematical description of the somatic model](#)”). There are only two

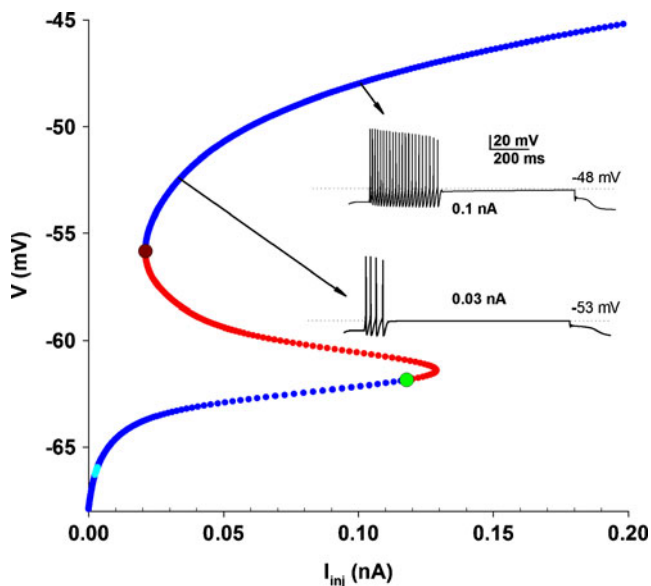


**Fig. 8** Stability of the equilibria of  $V$  versus  $I_{inj}$ . Cyan and blue points refer to asymptotically stable equilibria, red points indicate unstable equilibria, and non-hyperbolic equilibria are shown in green and brown

non-hyperbolic equilibria (green and brown points in Fig. 8), that arise when the system undergoes a bifurcation phenomenon (the numerical analysis suggests that the green point is a subcritical Hopf bifurcation point, i.e., a phenomenon which occurs when an unstable equilibrium becomes stable with the emergence of an unstable limit cycle (Rüdiger 2010)). All simulations showed that for any value of  $I_{inj}$  for which the neuron generates a train of spikes, the membrane potential  $V$  converges to an asymptotically stable value greater than  $-55.844$  mV (brown point in Fig. 8). Thus, the neuron dynamics would not be consistent with one of the major experimental findings, since the depolarization block will be reached for any input current generating spikes (see insets in Fig. 8), in striking contrast with experiments, where the depolarization block is reached only for relatively high values of  $I_{inj}$ .

This effect can be understood by considering the bistability region of the phase plane in the interval  $(0.021 \text{ nA}, 0.128 \text{ nA})$  of  $I_{inj}$ . In this region of the phase space, two asymptotically stable equilibria and one unstable equilibrium coexist with an unstable limit cycle. This result explains why this model, implemented by just isolating the soma from the rest of the neuron, cannot reproduce the experimental findings, but also indicates a way to better match the experimentally observed neuron dynamics.

We hypothesized that suitable modifications of the model parameters can change the shape of the  $V$ - $I_{inj}$  bifurcation diagram in such a way to achieve better agreement with experiments. For this reason, we explored the space of what we consider the minimum and most reasonable set of free parameters, i.e. the peak ionic conductances and the somatic capacitance, leaving all channel kinetics unaltered. The final set of

**Table 4** Somatic reduced model after parameters optimization (all values in mS/cm<sup>2</sup>)

Parameter	$\bar{g}_{NaT}$	$\bar{g}_{K_{DR}}$	$\bar{g}_{K_M}$	$\bar{g}_{CaL}$	$\bar{g}_{CaR}$	$\bar{g}_{mAHP}$
Morphological model	35	15	1.0	0.5	0.1	247.5
Somatic model	22	5	0.9	0.1	0.05	1

values is compared to that used for the full model in Table 4. These values were obtained using a total somatic capacitance of 120 pF, within the experimental range of 60–195 pF for CA1 neurons (Zemankovics et al. 2010; Scorza et al. 2011).

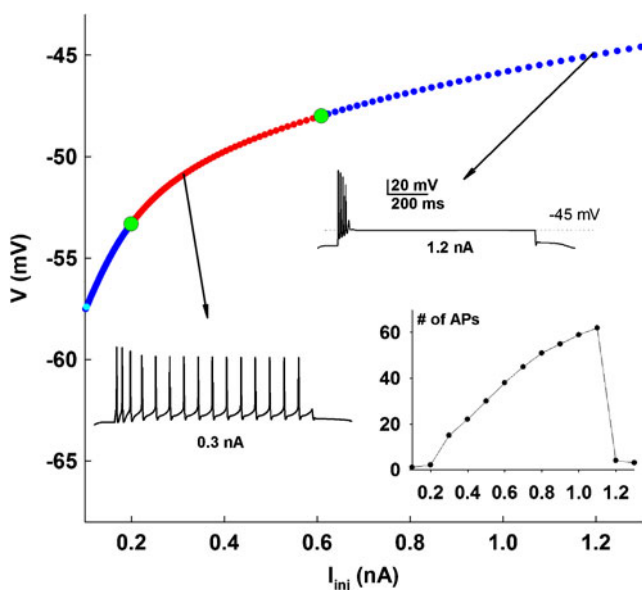
The new equilibria of  $V$  versus  $I_{inj}$  are plotted in Fig. 9. The new bifurcation diagram is very different with respect to the one obtained in the first stage. It now exhibits two Hopf bifurcation points (HB) (green in Fig. 9), and a single equilibrium value for  $V$  at any suprathreshold value of  $I_{inj}$ . The first HB point corresponds to a supercritical Hopf bifurcation, i.e., a phenomenon which occurs when a stable equilibrium point becomes unstable with the emergence of a stable limit cycle (Rüdiger 2010). Beyond it the neuron generates a regular train of spikes (Fig. 9, inset for  $I_{inj} = 0.3$  nA). The second green point leads to a subcritical Hopf bifurcation, i.e., a phenomenon that occurs when an unstable equilibrium becomes stable with emergence of an unstable limit cycle. In this last case, the amplitude of the oscillations decreases to zero and the membrane

potential reaches an equilibrium point on the blue line, i.e., depolarization block (see Fig. 9, inset for  $I_{inj} = 1.2$  nA). These two bifurcation phenomena are responsible for the different neuron dynamics, which are consistent with the experimental findings.

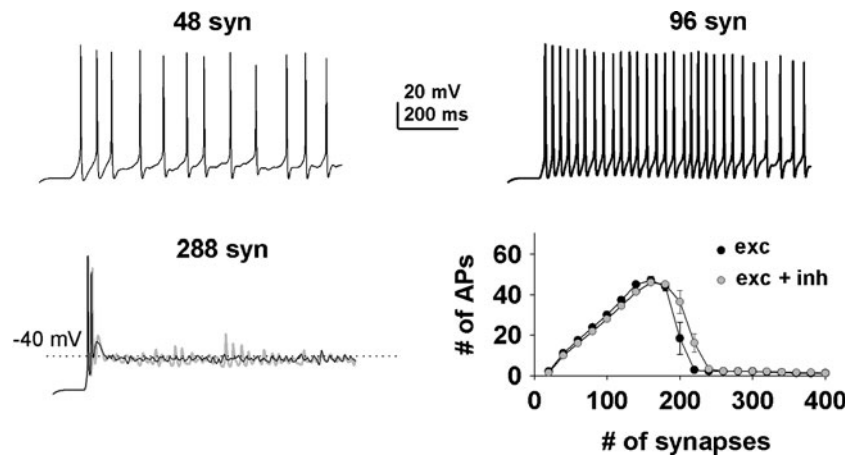
As mentioned before, in implementing large networks composed of single-compartment units instead of accurate morphological representations, it is important to ensure that the reduced system is able to reproduce the same features exhibited by the more complex neuron. Thus, in order to test if the depolarization block process was preserved in the presence of synaptic inputs in our somatic model too, we used the same protocol of stimulation as for the realistic neuron case and adjusted the peak synaptic conductance to see if the depolarization block could be achieved. We found that a ten-fold reduction of the peak synaptic conductance was enough to exhibit properties qualitatively similar to the realistic neuron case, as demonstrated by the typical model traces and the average number of spikes shown in Fig. 10. Taken together, these results suggest that it is possible to reduce a morphologically accurate neuron reconstruction to a single compartment model able to qualitatively reproduce the same firing features using the same set of conductances. This is an important step, since it might hopefully allow to build a large model network and in turn use it to make specific, experimentally testable predictions about the effects of channel manipulations.

### 3.2 Bifurcation analysis with respect to $V_{mNaT}^{1/2}$ and $V_{mK_{DR}}^{1/2}$

Motivated by the results using the morphological model, we next focused our attention on the role of the activation of  $NaT$  and  $K_{DR}$  currents, as the main mechanisms responsible for the depolarization block phenomenon. To this end, we performed a bifurcation analysis with respect to the parameters  $V_{mNaT}^{1/2}$  and  $V_{mK_{DR}}^{1/2}$ , to study their influence on the neuron dynamics as a function of the current injection. In Fig. 11(a) we show the stability character of the membrane potential as a function of  $V_{mNaT}^{1/2}$  and  $I_{inj}$ . In this plot, blue and cyan regions correspond to asymptotically stable steady-



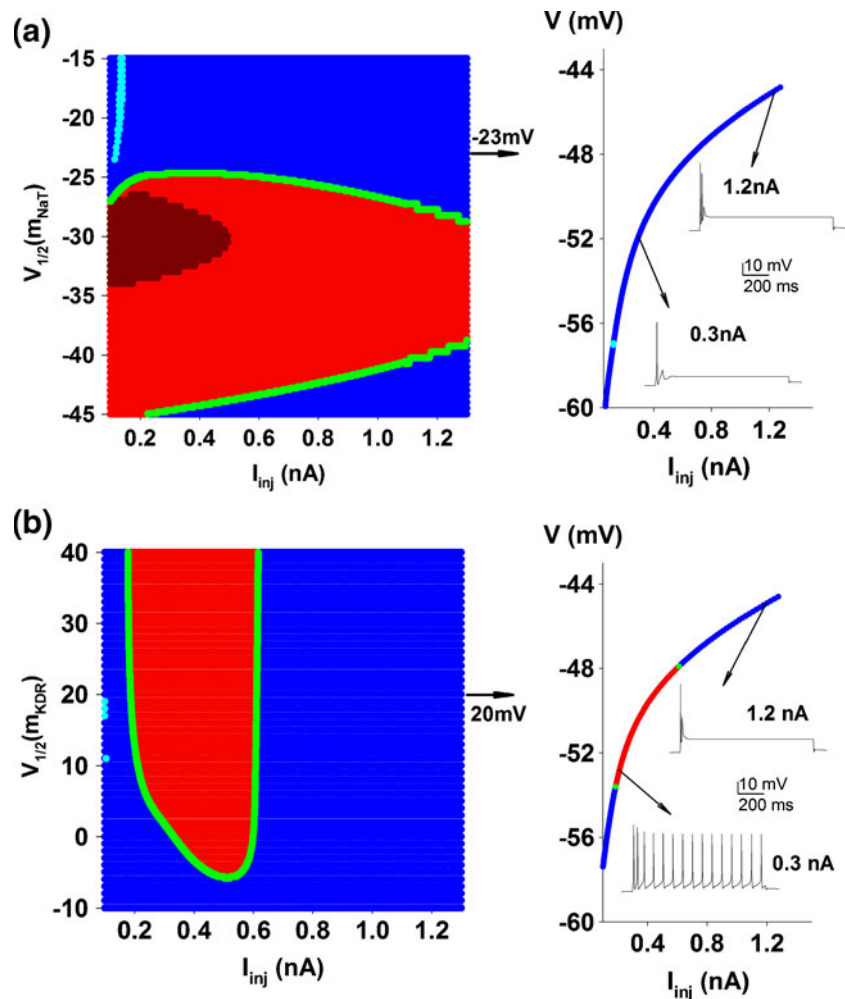
**Fig. 9** Stability of the equilibria of  $V$  versus  $I_{inj}$  after parameters optimization. Cyan and blue points refer to asymptotically stable equilibria, red points indicate unstable equilibria, and Hopf bifurcation points are shown in green



**Fig. 10** Representative single-compartment model response to random excitatory synaptic inputs. Typical membrane potential during sustained random synaptic activity (Poisson distribution) of different number of synapses, and number of action potentials

triggered in response to an increasing number of synapses. Traces and symbols in *black* show results using only excitatory inputs, those in *gray* show results with excitatory and inhibitory inputs

**Fig. 11** The 2-parameters bifurcation diagram after parameter optimization. **(a)** Dependence of the dynamical properties of the somatic model varying  $I_{inj}$  and  $V_{mNaT}^{1/2}$  in the intervals  $[0, 1.4]$  nA and  $[-45, -15]$  mV, respectively. **(b)** Dependence of the dynamical properties of the somatic model varying  $I_{inj}$  and  $V_{mKDR}^{1/2}$  in the intervals  $[0, 1.4]$  nA and  $[-10, 40]$  mV, respectively. Both the *cyan* and *blue points* refer to asymptotically stable equilibria. The *red* and *green points* are for unstable and non-hyperbolic equilibria, respectively





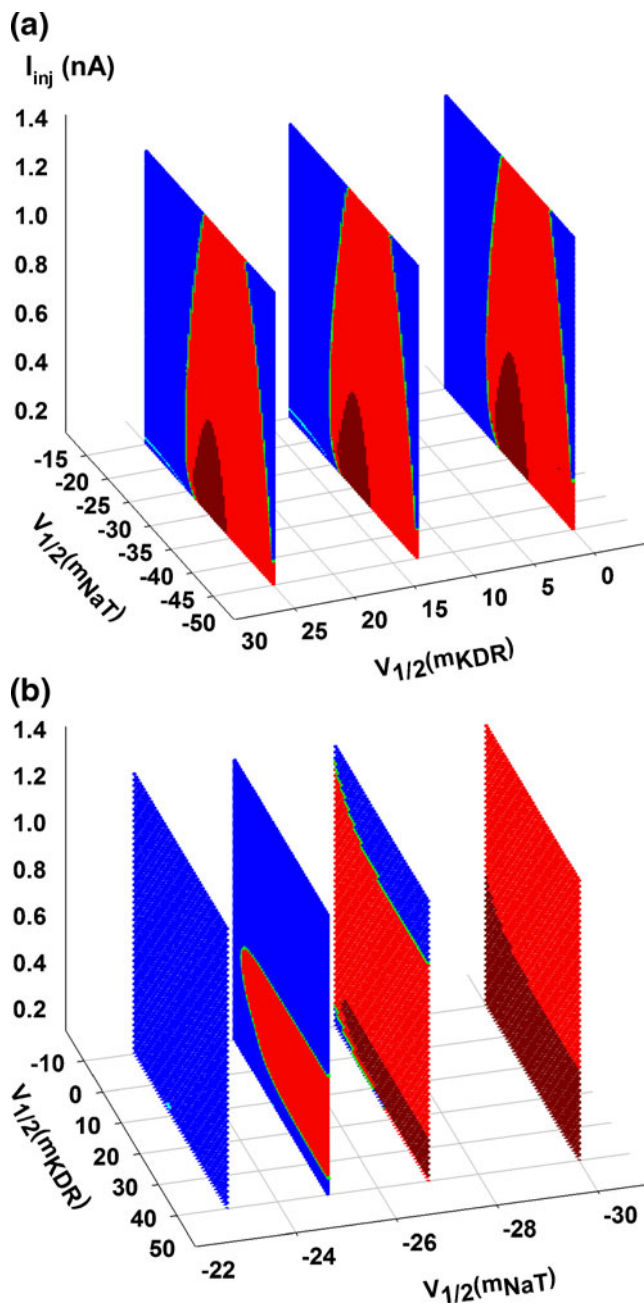


**Fig. 12** The 3-parameters bifurcation diagram after parameters' optimization. (a) Dependence of the dynamical properties of the somatic model for  $V_{mNaT}^{1/2} = 0, 13, 25$  mV, varying the parameters  $I_{inj}$  and  $V_{mNaT}^{1/2}$  in the intervals  $[0, 1.4]$  nA and  $[-45, -15]$  mV, respectively. (b) Dependence of the dynamical properties of the somatic model for  $V_{mNaT}^{1/2} = -30, -27, -25, -23$  mV, varying  $I_{inj}$  and  $V_{mKDR}^{1/2}$  in the intervals  $[0, 1.4]$  nA and  $[-10, 40]$  mV, respectively. Both the cyan and blue points refer to asymptotically stable equilibria. The red and green points are for unstable and non-hyperbolic equilibria, respectively

states, red and brown regions to unstable steady-states, and the green region corresponds to non-hyperbolic equilibria states. Different color regions correspond

to different firing behaviors, as discussed for Figs. 8 and 9.

We remark that the neuron exhibits a regular train of action potentials only if  $V_{mNaT}^{1/2}$  is such that the corresponding bifurcation diagram presents a supercritical Hopf bifurcation point before the red line of the unstable steady states. This is the case for our control model (Fig. 9). To highlight the different dynamics resulting from a slightly different value of  $V_{mNaT}^{1/2}$ , e.g.  $-23$  mV instead of the control value of  $-25$  mV, in Fig. 11(a) (right) we plot the bifurcation diagram for the equilibrium values of the membrane potential and two traces obtained at different values of  $I_{inj}$ . As can be seen, a relatively small change (a  $-2$  mV shift in the activation curve for  $Na^+$  in this case) is sufficient to enter a zone with no unstable steady-states: under this condition the neuron will show depolarization block for any suprathreshold value of  $I_{inj}$  (compare with traces in Fig. 9). The stability character of  $V$  as function of  $V_{mKDR}^{1/2}$  and  $I_{inj}$  is shown in Fig. 11(b). It can be easily recognized that the structure of the bifurcation diagram is such that the overall neuron dynamics will be the same for a relatively large range of  $V_{mKDR}^{1/2}$  values (i.e., for any value of  $V_{mKDR}^{1/2}$  such that the corresponding bifurcation diagram presents exactly two Hopf bifurcation points: the first one supercritical, and the second one subcritical), and particularly in the region above its control value of  $13$  mV. As shown in Fig. 11(b) (right), even a  $+7$  mV shift in the activation curve (from  $13$  to  $20$  mV) generated relatively little differences with control results (Fig. 9) for the equilibrium values, especially near the unstable steady-state region (red points). However, above this region, i.e. for higher  $I_{inj}$ , the reduced  $K_{DR}$  activation results in a reduced driving force for repolarization after each AP, and the neuron quickly reaches the depolarization block (see inset for  $I_{inj} = 1.2$  nA in Fig. 11(b), right).

The robustness of the stability properties for large changes of  $V_{mKDR}^{1/2}$  was confirmed by the bifurcation diagrams of  $V_{mNaT}^{1/2}$  obtained for different values of  $V_{mKDR}^{1/2}$ , shown in Fig. 12(a). There are no qualitative differences in their structure for a wide range of values tested for  $V_{mKDR}^{1/2}$  ( $0$ – $25$  mV). This is in contrast with the very sensitive bifurcation diagrams of  $V_{mKDR}^{1/2}$  obtained for different values of  $V_{mNaT}^{1/2}$ . In this case, illustrated in Fig. 12(b), just a few mV shift in the  $NaT$  activation curve can drastically change the bifurcation structure, for example by completely abolishing oscillations or depolarization block for depolarizing or hyperpolarizing shifts, respectively. This result suggests another experimentally testable prediction: the  $NaT$



activation curve in CA1 neurons should be shifted towards a more depolarized potential in those neurons where the depolarization block occurs for lower inputs.

#### 4 Discussion

The experimental results at the core of this paper highlight a phenomenon rarely considered in the literature, namely that of depolarization block: the action potentials amplitude of CA1 neurons during a relatively high and sustained somatic current injection decreases and tends to zero, with the membrane potential reaching an equilibrium value between  $-40$  mV and  $-35$  mV, above the spike threshold.

Pinsky and Rinzel (1994) have already shown that a spatially reduced version of Traub's CA3 model (Traub et al. 1991), Traub and Wong (1982) can preserve most of the essential features of a morphological-like model. In spite of their generality, detailed morphological models present some shortcomings, such as the practical impossibility to perform a detailed mathematical investigation of the parameter space, and very high computational requirements in a network. Consequently, several Hodgkin–Huxley-type models have been proposed in the literature to describe the neuronal dynamics using simplified formulations (Golomb et al. 2006; Pospischil et al. 2008; Nowacki et al. 2011; Meng et al. 2011) (and references therein for single-compartment models). To the best of our knowledge, ours is the only single-compartment model derived from a realistic set of conductances that is able to exhibit a dynamics towards the depolarization block consistent with experimental findings.

Realistic models of CA1 neurons have so far ignored the depolarization block, probably misled by the lack of specific interest in the experimental field. Here we have explored the mechanisms underlying the depolarization block in a realistic model and its reduction to a single compartment system. The model highlighted the key role of sodium and DR-type potassium activation, suggesting specific properties without which the depolarization block cannot be reproduced. In addition to the obvious role for the  $Na^+$  current, the unique role of  $K_{DR}$  should be stressed. None of the other major potassium conductances expressed in these neurons have kinetic properties consistent with the possibility to enter a depolarization block. In fact, each has a property that would hinder the dynamics to depolarization block, and would generate model traces inconsistent with one or more experimentally observed features.

For example, the transient nature of  $K_A$  would reduce the  $K^+$  current, resulting in a large depolarization; the relatively long  $K_M$  time constant would generate depolarization a block for any suprathreshold value of current injection; the Ca-dependent  $K^+$  currents would either generate too much hyperpolarization following  $Ca^{2+}$  entry during a train of APs, or be inactivated after 100–200 ms following  $Ca^{2+}$  extrusion. However, for the M-type potassium and the medium fast-AHP, our model predicts a specific role in determining the membrane potential equilibrium value observed in the experiments. This role can be experimentally tested by blocking one or both of these currents to test for a depolarizing shift in the equilibrium value.

We assume that the depolarization block is typically not reported or discussed in experimental findings because the range of input current in which it occurs is considered unphysiological. However, our model suggested that background synaptic activity in the gamma range involving less than 3% of the total number of excitatory synaptic inputs converging on any given CA1 pyramidal neuron, could easily generate an aggregate peak input current larger than 1 nA. This makes the depolarization block an important property of a neuron, since in a large active network several neurons will likely be in a depolarization block at any given time. Their (not) firing behavior would then be drastically different with respect to neurons that, by not taking into account the depolarization block, would keep firing at high rates. We suggest that this state should be explicitly taken into account by computational models at all scales of implementation. From this point of view, this is the first time that a realistic set of ionic currents, used to implement both a morphological accurate neuron and a single-compartmental model, is shown to be in very good agreement with experimental findings including the depolarization block.

Finally, in hippocampal pyramidal CA1 neurons many membrane mechanisms (reviewed in Migliore and Shepherd 2002, 2005) seem to be exquisitely tailored to prevent the generation of too many spikes, especially in the dendrites. For example, dendritic slow sodium inactivation (Spruston et al. 1995; Migliore 1996), somatodendritic sodium channels activation shifted towards more depolarized values with respect to axonal channels (Colbert and Pan 2002), and the increasing density of  $K_A$  channels with distance from soma (Hoffman et al. 1997; Migliore et al. 1999), all reduce the possibility for a CA1 neuron to generate and propagate a long train of APs in the soma and dendrites, thus protecting the cell from firing at high frequency. The depolarization block appears to

be one additional mechanism along the same route, and it may be relevant in modulating the initiation and spread of focal epileptic seizures, which generate a paroxysmal depolarizing shift in the involved neurons that may be large enough to inactivate  $Na^+$  channels (Dichter and Ayala 1987; Ayala et al. 1973; McCormick and Contreras 2001). From this point of view, we note that the voltage equilibrium point during the depolarization block in a healthy neuron is around  $-40$  mV, which is dangerously close to the about  $-35$  mV threshold needed for glutamate release even in the absence of an action potential (Xiong and Chen 2002). Neurons with a relatively high  $V_{eq}$ , caused for example by a low density of  $K_M$  or  $Ca$ -dependent  $K^+$  channels, may thus be more easily involved in originating or spreading seizures. We thus suggest that this state, and the physiological conditions leading to it, should be one of the mechanisms systematically characterized in experiments studying modulations of the electrophysiological and firing properties of CA1 neurons.

**Acknowledgements** Financial support from “Compagnia di San Paolo” is gratefully acknowledged. We thank Drs. S. Cuomo and P. De Michele (Department of Mathematics and Applications “Renato Caccioppoli”, University of Naples Federico II) for assistance in running the parallel version of our morphological model and for the use of the S.Co.P.E. Grid infrastructure of University of Naples Federico II.

## Appendix

### Ionic currents

The full morphological model includes the following 17 types of ionic channels, most of them distributed non-uniformly along the somatodendritic region. More precisely, the  $K_M$  and  $K_A$  potassium currents are those described by Shah et al. (2008), whereas the other types

of currents have been distributed as in model of Poirazi et al. (2003b).

- Soma: a leak current, a transient sodium ( $NaT$ ) current, a delay-rectifier potassium ( $K_{DR}$ ) current, an A-type potassium current ( $K_A$ ), a M type potassium current ( $K_M$ ), a mixed conductance hyperpolarization activated h-current, three types of voltage dependent calcium currents (namely  $LVA$  T-type current, a  $HVA$  R-type current, a  $HVA$  L-type current), two types of calcium dependent potassium currents (a slow  $AHP$  current and a medium fast  $AHP$  current);
- Axon: a  $NaT$  current, a  $K_{DR}$  current, a leak current, a  $K_A$  current and  $K_M$  current;
- Basal dendrites: a  $NaT$  current, a  $K_{DR}$  current, a leak current, a  $K_A$  current and a h-current;
- Apical trunk: all currents included in the soma with the exception of  $K_M$  current and the insertion of a  $K_A$  current (the  $HVA$  R and L type are different from those in soma);
- Apical dendrites: all currents included in the apical trunk with an insertion of a persistent sodium current.

Ionic currents were modeled following a Hodgkin-Huxley-like formalism as follows:

$$I_j = \bar{g}_j m_j^{a_j} h_j^{b_j} (V - E_j), \quad (2)$$

where  $\bar{g}_j$  represents the maximal ionic conductance,  $(m_j, h_j)$  and  $(a_j, b_j)$  are the gating variables for activation and inactivation and their exponents, respectively, and  $E_j$  is the reversal potential associated with the particular ion or ions that make up the current. The dynamics of the gating variables  $(m_j, h_j)$  is governed by an ODE of the form

$$\frac{d\chi}{dt} = \frac{\chi_\infty - \chi}{\tau_\chi} \quad (3)$$

where the activation and inactivation steady-state functions  $\chi_\infty$ , and their time constant  $\tau_\chi$  are given by

$$\chi_\infty = \frac{\alpha_\chi(V)}{\alpha_\chi(V) + \beta_\chi(V)}, \quad \chi_\infty = \frac{1}{1 + \exp\left[\left(V - V_\chi^{1/2}\right)/k_\chi\right]}, \quad (4)$$

$$\tau_\chi = \frac{Q}{\alpha_\chi(V) + \beta_\chi(V)}, \quad (5)$$

$$\tau_\chi = \tau_\chi^0 + \frac{\bar{\tau}_\chi}{G_\chi \left( \exp\left[\gamma_\chi \left(V - V_\chi^{1/2}\right)/\tilde{k}_\chi\right] + \exp\left[(\gamma_\chi - 1) \left(V - V_\chi^{1/2}\right)/\tilde{k}_\chi\right] \right)}, \quad (6)$$

In the following subsections we report only the kinetic details of the currents directly involved with the results

discussed in this paper. The parameters of all the other currents were not modified from their original values.

### Transient $NaT$ current

The  $NaT$  current was implemented according to Shah et al. (2008), so Eq. (2) becomes:

$$I_{NaT} = \bar{g}_{NaT} m_{NaT}^3 h_{NaT} (V - 50). \quad (7)$$

The dynamics of the gating variable  $m_{NaT}$  is described by Eqs. (3), (4)<sub>1</sub> and (5) as follows

$$\alpha_{m_{NaT}} = \begin{cases} \frac{0.4 (V - V_{m_{NaT}}^{1/2})}{1 - \exp[-(V - V_{m_{NaT}}^{1/2})/k_{m_{NaT}}]}, \\ |V - V_{m_{NaT}}^{1/2}| > 10^{-6} \text{ mV} \\ 0.4 k_{m_{NaT}}, & \text{otherwise} \end{cases},$$

$$\beta_{m_{NaT}} = \begin{cases} \frac{-0.124 (V - V_{m_{NaT}}^{1/2})}{1 - \exp[(V - V_{m_{NaT}}^{1/2})/k_{m_{NaT}}]}, \\ |V_{m_{NaT}}^{1/2} - V| > 10^{-6} \text{ mV} \\ 0.124 k_{m_{NaT}}, & \text{otherwise} \end{cases},$$

$$\tau_{m_{NaT}} = \begin{cases} \frac{3}{\alpha_{m_{NaT}}(V) + \beta_{m_{NaT}}(V)}, \\ \frac{3}{\alpha_{m_{NaT}}(V) + \beta_{m_{NaT}}(V)} > 0.02 \text{ ms} \\ 0.02 \text{ ms}, & \text{otherwise} \end{cases},$$

The dynamics of the gating variable  $h_{NaT}$  is described by Eqs. (3), (4)<sub>2</sub>, and (5), i.e.,

$$(h_{NaT})_{\infty} = \frac{1}{1 + \exp[(V - V_{h_{NaT}}^{1/2})/k_{h_{NaT}}]},$$

$$\alpha_{h_{NaT}} = \begin{cases} \frac{0.03 (V + 45)}{1 - \exp[-(V + 45)/1.5]}, \\ |V - V_{h_{NaT}}^{1/2}| > 10^{-6} \text{ mV} \\ 0.045, & \text{otherwise} \end{cases},$$

$$\beta_{h_{NaT}} = \begin{cases} \frac{-0.01 (V + 45)}{1 - \exp[(V + 45)/1.5]}, \\ |V_{h_{NaT}}^{1/2} - V| > 10^{-6} \text{ mV} \\ 0.015, & \text{otherwise} \end{cases}$$

All the parameters written in this section are listed in Table 3.

### The delayed rectifier $K^+$ current

The delayed rectifier  $K^+$  current ( $I_{KDR}$ ) taken from Shah et al. (2008) is given by:

$$I_{KDR} = \bar{g}_{KDR} m_{KDR} (V + 77) \quad (8)$$

The dynamics of  $m_{KDR}$  is described by Eqs. (3), (4)<sub>2</sub> and (6), with  $V_{m_{KDR}}^{1/2} = 13 \text{ mV}$ ,  $k_{KDR} = -8.824 \text{ mV}$ ,  $\tau_{m_{KDR}}^0 = 0 \text{ ms}$ ,  $\gamma_{m_{KDR}} = 0.7$ ,  $G_{KDR} = 1$ ,  $\bar{\tau}_{m_{KDR}} = \frac{1}{0.02} \text{ ms}$ ,  $\bar{k}_{s_{NaT}} = 8.824 \text{ mV}$ , and a minimum value for  $\tau_{m_{KDR}}$  of 2 ms.

### The potassium M-type current

The M current ( $I_{KM}$ ) was modeled according to Shah et al. (2008), namely

$$I_{KM} = \bar{g}_{KM} m_{KM} (V + 77) \quad (9)$$

The dynamics of the gating variable  $m_{KM}$  is described by Eqs. (3), (6) and (4)<sub>2</sub> with the following formula:

$$(m_{KM})_{\infty} = \frac{1}{1 + \exp[(V - V_{m_{KM}}^{1/2})/(k_{m_{KM}})]} \quad (10)$$

Some parameters are listed in Table 3 and the others are set as follows:  $\tau_{m_{KM}}^0 = 60 \text{ ms}$ ,  $G_{m_{KM}} = 1$ .

### The m-type Ca-dependent potassium current, mAHP

The medium AHP current  $I_{mAHP}$ , from Moczydlowski and Latorre (1983), is given by

$$I_{mAHP} = \bar{g}_{mAHP} m_{mAHP} (V + 77) \quad (11)$$

The dynamics of the gating variable  $m_{mAHP}$  is described by Eqs. (3), (4)<sub>1</sub> and (5). The  $\alpha_m$  and  $\beta_m$  are given by:

$$\alpha_{mAHP} = \frac{0.48}{1 + \frac{0.18}{[Ca^{2+}]_i} \exp[-2d_1 V \cdot 37.775]},$$

$$\beta_{mAHP} = \frac{0.28}{1 + \frac{[Ca^{2+}]_i}{0.011 \exp[-2d_2 V \cdot 37.775]}} \quad (12)$$

$[Ca^{2+}]_i$  is the internal calcium concentration, and the other parameters are listed in Table 3.

### Mathematical description of the somatic model

We recall that the single-compartment model takes into account only the ten somatic ionic currents listed in Section “**Ionic currents**”, i.e.,

- one transient  $Na^+$  current  $I_{NaT}$ ;
- three  $K^+$  currents: one delayed rectifier  $I_{KDR}$ , one muscarinic-sensitive  $I_{KM}$ , and one A-type  $I_{KA}$ ;

- three  $Ca^{2+}$  currents: one LVA T-type current  $I_{CaT}$ , one HVA R-type current  $I_{CaR}$ , and one HVA L-type current  $I_{CaL}$ ;
- one  $h$  current  $I_h$ ;
- two  $Ca^{2+}$ -activated  $K^+$  currents: one slow  $I_{sAHP}$ , and one medium  $I_{mAHP}$ .

Then, the current balance equation for the somatic membrane potential  $V$  becomes

$$C_m \frac{dV}{dt} = -I_{NaT} - I_{KDR} - I_{KM} - I_{KA} - I_{CaT} - I_{CaR} - I_{CaL} - I_h - I_{sAHP} - I_{mAHP} - I_{leak} + I_{inj}. \quad (13)$$

Thus, closing the membrane equation (13) with the ionic currents, the dynamics of gating variables, and the intracellular  $Ca^{2+}$  concentration,  $[Ca^{2+}]_i$ , the model consists of a system of seventeen nonlinear ODEs in the unknown functions

$$V, m_{NaT}, h_{NaT}, s_{NaT}, m_{KDR}, m_{KM}, m_{KA}, h_{KA}, m_{CaT}, h_{CaT}, m_{CaR}, h_{CaR}, m_{CaL}, m_h, m_{sAHP}, m_{mAHP}, [Ca^{2+}]_i. \quad (14)$$

The model is analytically intractable, and solutions may be obtained only by numerical integration. The Cauchy problem for our model is:

$$\begin{cases} \frac{d\mathbf{X}}{dt} = \mathbf{f}(\mathbf{X}, I_{ext}), \\ \mathbf{X}(0, I_{ext}) = \mathbf{X}_0(I_{ext}), \end{cases} \quad (15)$$

where the components of the vector  $\mathbf{X}$  are listed in Eq. (14), and  $\mathbf{f}(\mathbf{X}, I_{ext})$  is the vector whose components are the functions in the right-hand side of the ODEs. In addition, we set

$$f_1(\mathbf{X}, I_{ext}) = I_{ext} - G(\mathbf{X}). \quad (16)$$

In order to compare our dynamical model with experiments, we have to fix the values of all parameters and the external current. We set the potential  $V$  to the resting value  $V_{rest}$  and all the gating variables and

intracellular  $Ca^{2+}$  concentration to the corresponding steady-state values, i.e.,

$$X_{j,0} = \begin{cases} V_{rest} & j = 1, \\ X_j^\infty(V_{rest}) & j = 2, \dots, 14, \\ m_{sAHP}^\infty([Ca^{2+}]_i^\infty) & j = 15, \\ m_{mAHP}^\infty(V_{rest}, [Ca^{2+}]_i^\infty) & j = 16, \\ [Ca^{2+}]_i^\infty & j = 17, \end{cases} \quad (17)$$

where  $[Ca^{2+}]_i^\infty$  is a solution of the nonlinear equation

$$f_{17}(V_{rest}, m_{CaL}^\infty, m_{CaR}^\infty, h_{CaR}^\infty, [Ca^{2+}]_i) = 0. \quad (18)$$

For the all simulations in Section 3.1.3 we have set the initial data as in Eq. (17) in which  $V_{rest} = -70$  mV.

A fundamental step in the qualitative analysis of our dynamical system is finding the equilibria. To start with, we calculate and characterize the stationary states  $\mathbf{X}^*$  which are defined by the condition  $\mathbf{f}(\mathbf{X}^*, I_{ext}) = 0$ . As in the Hodgkin–Huxley-type models, a suitable numerical procedure was applied to reduce the vectorial equation  $\mathbf{f}(\mathbf{X}^*, I_{ext}) = 0$  to the nonlinear scalar equation

$$f_1(\mathbf{X}^*, I_{ext}) = I_{ext} - g(V^*) = 0, \quad (19)$$

where  $g(V) = G(V, X_2^\infty(V), \dots, X_{17}^\infty(V))$ . Owing to the presence of the calcium currents, the last three equations for the equilibria become

$$\begin{aligned} f_{15}(m_{sAHP}^*, [Ca^{2+}]_i^*) &= 0, \\ f_{16}(m_{mAHP}^*, V^*, [Ca^{2+}]_i^*) &= 0, \\ f_{17}(V^*, m_{CaL}^*, m_{CaR}^*, h_{CaR}^*, [Ca^{2+}]_i^*) &= 0, \end{aligned} \quad (20)$$

consequently a nonstandard numerical procedure was applied to derive Eq. (19). This last equation, which supplies the stationary point  $\mathbf{X}^*$  as a function of  $I_{ext}$ , can be solved only numerically. Linearizing the  $\mathbf{f}(\mathbf{X}^*, I_{ext})$  around the stationary states, we investigated their stability properties by varying the external current  $I_{ext}$ . The stability of the equilibria is characterized

by the eigenvalues  $\lambda_1, \dots, \lambda_{17}$  of the usual Jacobian matrix

$$J(I_{\text{ext}}) = \frac{\partial f_j}{\partial X_k}(\mathbf{X}^*, I_{\text{ext}}), \quad (21)$$

and all bifurcations diagrams are obtained using the procedure originally introduced by Troy for the Hodgkin–Huxley model in Troy (1974) (see also Hassard 1978; Troy 1978).

## References

- Andrasfalvy, B. K., & Magee, J. C. (2001). Distance-dependent increase in AMPA receptor number in the dendrites of adult hippocampal CA1 pyramidal neurons. *Journal of Neuroscience*, 21, 9151–9159.
- Ayala, G. F., Dichter, M., Gumnit, R. J., Matsumoto, H., & Spencer, W. A. (1973). Genesis of epileptic interictal spikes. New knowledge of cortical feedback systems suggests a neurophysiological explanation of brief paroxysms. *Brain Research*, 52, 1–17.
- Colbert, C. M., & Pan, E. (2002). Ion channel properties underlying axonal action potential initiation in pyramidal neurons. *Nature Neuroscience*, 5, 533–538.
- Dichter, M. A., & Ayala, G. F. (1987). Cellular mechanisms of epilepsy: A status report. *Science*, 237, 157–164.
- Gasparini, S., & Magee, J. C. (2002). Phosphorylation-dependent differences in the activation properties of distal and proximal dendritic  $\text{Na}^+$  channels in rat CA1 hippocampal neurons. *Journal of Physiology*, 541.3, 665–672.
- Golomb, D., Yue, C., & Yaari, Y. (2006). Contribution of persistent  $\text{Na}^+$  current and M-type  $\text{K}^+$  current to somatic bursting in CA1 pyramidal cells: Combined experimental and modeling study. *Journal of Neurophysiology*, 96, 1912–1926.
- Hassard, B. (1978). Bifurcation of periodic solutions of the Hodgkin–Huxley model for the squid giant axon. *Journal of Theoretical Biology*, 71, 401–420.
- Hemond, P., Epstein, D., Boley, A., Migliore, M., Ascoli, G. A., & Jaffe, D. B. (2008). Distinct classes of pyramidal cells exhibit mutually exclusive firing patterns in hippocampal area CA3b. *Hippocampus*, 18, 411–424.
- Hines, M. L., & Carnevale, N. T. (2003). The NEURON simulation environment. In *The handbook of brain theory and neural networks* (2nd ed., pp. 769–773). Cambridge: MIT Press.
- Hoffman, D. A., & Johnston, D. (1998). Downregulation of transient  $\text{K}^+$  channels in dendrites of hippocampal CA1 pyramidal neurons by activation of PKA and PKC. *Journal of Neuroscience*, 18, 3521–3528.
- Hoffman, D. A., Magee, J. C., Colbert, C. M., & Johnston, D. (1997).  $\text{K}^+$  channel regulation of signal propagation in dendrites of hippocampal pyramidal neurons. *Nature*, 387, 869–875.
- Ito, H., & Schuman, E. M. (2009). Distance-dependent homeostatic synaptic scaling mediated by A-type potassium channels. *Frontiers in Cellular Neuroscience*, 3, 1–15.
- Jiang, L., Sun, S., Nedergaard, M., & Kang, J. (2000). Paired pulse modulation at individual GABAergic synapses in rat hippocampus. *Journal of Physiology*, 523.2, 425–439.
- Koch, C. (1999). *Biophysics of computation: Information processing in single neurons*. New York: Oxford University Press.
- Magee, J. C. (1998). Dendritic hyperpolarization-activated currents modify the integrative properties of hippocampal CA1 pyramidal neurons. *Journal of Neuroscience*, 18, 7613–7824.
- Marasco, A., & Romano, A. (2001). *Scientific computing with mathematica: Mathematical problems for ordinary differential equations*. Boston: Birkhauser. ISBN 0-8176-4205-6.
- Marie, H., Morishita, W., Yu, X., Calakos, N., & Malenka, R. C. (2005). Generation of silent synapses by acute *in vivo* expression of CaMKIV and CREB. *Neuron*, 45, 741–752.
- McCormick, D. A., & Contreras, D. (2001). On the cellular and network bases of epileptic seizures. *Annual Review of Physiology*, 63, 815–846.
- Megias, M., Emri, Z., Freund, T. F., & Gulyás, A. I. (2001). Total number and distribution of inhibitory and excitatory synapses on hippocampal CA1 pyramidal cells. *Neuroscience*, 102, 527–540.
- Meng, X., Lu, Q., & Rinzel, J. (2011). Control of firing patterns by two transient potassium currents: Leading spike, latency, bistability. *Journal of Computational Neuroscience*, 31, 117–136.
- Migliore, M. (1996). Modeling the attenuation and failure of action potentials in the dendrites of hippocampal neurons. *Biophysical Journal*, 71, 2394–2403.
- Migliore, M., Hoffman, D., Magee, J., & Johnston, D. (1999). Role of an A-type  $\text{K}^+$  conductance in the back-propagation of action potentials in the dendrites of hippocampal pyramidal neurons. *Journal of Computational Neuroscience*, 7, 5–15.
- Migliore, M., & Shepherd, G. M. (2002). Emerging rules for the distributions of active dendritic conductances. *Nature Reviews. Neuroscience*, 3, 362–370.
- Migliore, M., & Shepherd, G. M. (2005). Opinion: An integrated approach to classifying neuronal phenotypes. *Nature Reviews. Neuroscience*, 6, 810–818.
- Moczydlowski, E., & Latorre, R. (1983). Gating kinetics of  $2^+$ -activated  $\text{K}^+$  channels from rat muscle incorporated into planar lipid bilayers. *Journal of General Physiology*, 82, 511–542.
- Nowacki, J., Osinga, H. M., Browne, J. T., Randall, A. D., & Tsaneva-Atanasova, K. (2011). A unified model of CA1/3 pyramidal cells: An investigation into excitability. *Progress in Biophysics and Molecular Biology*, 105, 34–48.
- Pinsky, P. F., & Rinzel, J. (1994). Intrinsic and network rhythmicogenesis in a reduced Traub model for CA3 neurons. *Journal of Computational Neuroscience*, 1, 39.
- Poirazi, P., Brannon, T., & Mel, B. W. (2003). Arithmetic of subthreshold synaptic summation in a model CA1 pyramidal cell. *Neuron*, 37, 977–987.
- Poirazi, P., Brannon, T., & Mel, B. W. (2003). Pyramidal neuron as 2-layer neural network. *Neuron*, 37, 989–999.
- Pospischil, M., Toledo-Rodriguez, M., Monier, C., Piwkowska, Z., Bal, T., Frégnac, Y., et al. (2008). Minimal Hodgkin–Huxley type models for different classes of cortical and thalamic neurons. *Biological Cybernetics*, 99, 427–441.
- Remy, S., Beck, H., & Yaari, Y. (2010). Plasticity of voltage-gated ion channels in pyramidal cell dendrites. *Current Opinion in Neurobiology*, 20, 503–509.
- Rüdiger, S. (2010). Practical bifurcation and stability analysis practical bifurcation and stability analysis. In *Springer series: Interdisciplinary applied mathematics* (Vol. 5, 3rd ed.). New York: Springer.
- Samsonovich, A. V., & Ascoli, G. A. (2005). Statistical determinants of dendritic morphology in hippocampal pyramidal neurons: A hidden Markov model. *Hippocampus*, 15, 166–183.



- Scorza, C. A., Araujo, B. H., Leite, L. A., Torres, L. B., Otalora, L. F., Oliveira, M. S., et al. (2011). Morphological and electrophysiological properties of pyramidal-like neurons in the stratum oriens of Cornu ammonis 1 and Cornu ammonis 2 area of *Proechimys*. *Neuroscience*, 177, 252–268.
- Shah, M. M., Migliore, M., Valencia, I., Cooper, E. C., & Brown, D. A. (2008). Functional significance of axonal Kv7 channels in hippocampal pyramidal neurons. *Proceedings of the National Academy of Sciences of the United States of America*, 105, 7869–7874.
- Spruston, N., Schiller, Y., Stuart, G., & Sakmann, B. (1995). Activity-dependent action potential invasion and calcium influx into hippocampal CA1 dendrites. *Science*, 268, 297–300.
- Traub, R. D., & Wong, R. K. (1982). Cellular mechanism of neuronal synchronization in epilepsy. *Science*, 216, 745–747.
- Traub, R. D., Wong, R. K., Miles, R., & Michelson, H. (1991). A model of a CA3 hippocampal pyramidal neuron incorporating voltage-clamp data on intrinsic conductances. *Journal of Neurophysiology*, 66, 635–650.
- Troy, W. C. (1974). *Oscillatory phenomena in nerve conduction equations*. Ph.D. dissertation, SUNY at Buffalo.
- Troy, W. C. (1978). The bifurcation of periodic solutions in the Hodgkin–Huxley equations. *Quarterly of Applied Mathematics*, 36, 73–83.
- Xiong, W., & Chen, W. R. (2002). Dynamic gating of spike propagation in the mitral cell lateral dendrites. *Neuron*, 34, 115–126.
- Zemankovics, R., Káli, S., Paulsen, O., Freund, T. F., & Hájos, N. (2010). Differences in subthreshold resonance of hippocampal pyramidal cells and interneurons: The role of h-current and passive membrane characteristics. *Journal of Physiology*, 588(12), 2109–2132.